



Microstructure and Mechanical Properties of Millimeter WC Particle-Reinforced High-Chromium Cast Iron Composites

Ping Li, Xiao Li, Yongcun Li, Mengying Gong, Chen Tian, and Weiping Tong

(Submitted May 16, 2019; in revised form November 6, 2019; published online December 3, 2019)

WC particle/HCCI composites were prepared using liquid-phase sintering technology. In this study, millimeter WC particles were used to ensure that minimal WC particle performance was compromised during the preparation process. Moreover, with the aim of controlling the evolution of microstructures and secondary carbide precipitation in the matrix, different heat treatment methods were adopted in the manufacturing process. The microstructures of the composites were investigated via SEM, XRD, EPMA and TEM. The results showed that perfect metallurgical bonding was formed between the LCS and the WC/HCCI composites, and the width of the diffusion layer was 120 to 129 μm after heat treatment. A large number of secondary carbides precipitated in the matrix during heat treatment, and martensite formation occurred in the matrix during the subsequent cooling process, which effectively increased the micro-hardness of the matrix. The impact toughness of the LCS-toughened composites after heat treatment was 1.6 times that of the WC/HCCI composites, and the shear strength was 5 times that of the as-cast composites. The wear resistance of the composites under quenching at 950 °C and tempering at 220 °C was 5 times that of the as-cast composites.

Keywords abrasive wear, heat treatment, high-chromium cast iron, mechanical properties, microstructure, millimeter WC particles

1. Introduction

WC particle-reinforced high-chromium cast iron matrix composites have attracted extensive attention due to their excellent comprehensive properties. This kind of composite material has been widely used in metallurgy, mining, coal, chemical and other wear-resistant industries. The main reason is the combination of the high toughness of the metal matrix and the high wear resistance of reinforced ceramics (Ref 1). These composites are expected to replace traditional metal materials in many industrial fields.

Since WC particles have extremely high hardness, a high melting point, good wettability with molten metal and good wear resistance, the interface of the particle-reinforced composites is good (Ref 2). Moreover, the size of WC particles is also a key factor in the preparation of composites (Ref 3). When the particle size is small, the melting degree of the particles increases in the high-temperature liquid region, and most or even all of the WC particles are melted and diffused, which causes the original excellent properties to be lost. When

the particle size is large, the melting solution reacts excessively with the particles. This results in a large interface width and a greater loss of WC particles.

WC particles can be used as wear-resistant reinforcing phases for various metal surfaces or metal composites (Ref 4, 5), such as WC/steel and WC/Ni composites (Ref 6). Compared with other matrices of WC particle-reinforced composites, iron matrix composites have lower prices and better mechanical properties. High-chromium cast iron (HCCI) is considered a traditional wear-resistant composite. Generally, the microstructure of the carbides is determined by their type, volume fraction and morphology (Ref 7). On the other hand, the particularly hard matrix can also be changed by quenching and tempering with conventional heat treatment; thus, the transformation of austenite into martensite occurs in the matrix, while there are a large number of fine secondary carbides that precipitate (Ref 8).

Some scholars have used various methods to prepare WC particle-reinforced metal matrix composites. For example, WC-10Ti and WC-10V cermets were prepared by spark plasma sintering at a high temperature by Ehsan Ghasali et al. The results of the brittle fracture behavior showed that the bending strength of the WC-10V specimen was 613 ± 25 MPa, while the hardness of the WC-10Ti specimen was 3128 ± 42 Vickers (Ref 9). Zhou et al. used a vacuum infiltration casting technique to prepare WC particle-reinforced composites on the surface of gray cast iron, in which the volume fraction of WC particles reached up to 52% (Ref 4). Scholars have also adopted many other preparation methods, such as selective laser sintering (Ref 10), vacuum evaporative patterning (Ref 11), plasma melt injecting (Ref 10), sintering and laser cladding (Ref 12-14), and so on. In this study, WC particle-reinforced HCCI matrix composites were prepared by liquid-phase sintering (LPS). LPS is recognized as an important role in the preparation of particle-reinforced iron matrix composites (Ref 15, 16). This method produces a sufficient liquid phase to encapsulate the WC

Ping Li, Xiao Li, Yongcun Li, Mengying Gong, Chen Tian, and Weiping Tong, Key Laboratory of Electromagnetic Processing of Materials, Northeastern University, Shenyang 110819, China. Contact e-mails: holidaybwping@163.com, 289964012@qq.com, YC_Lee1988@163.com, gongmy1222@163.com, 1211967791@qq.com, and wptong@mail.neu.edu.cn.

particles, which can greatly improve the volume shrinkage rate of the resulting composites (Ref 17). By controlling the heating rate, heating temperature, holding time, cooling rate and other parameters (Ref 18), the interface width between the WC particles and the HCCI matrix was effectively controlled.

There is little information regarding the influence of millimeter WC particles on the preparation of composites and which processing technique should be used to achieve optimum wear properties of the composites. The presence of WC particles improves the wear resistance in different ways: by forming other carbides in the matrix, such as MC, M₂C, or M₆C; or the hardness of the matrix can be improved by the formation of higher martensite amounts (Ref 28). In addition, edge dissolution of WC particles with larger sizes during the preparation process and the interface width can be effectively controlled by controlling the preparation process parameters. Therefore, without sacrificing the mechanical properties of the original WC particles, an attempt was made to achieve a size of WC particles between 2 and 3 mm, and the LPS process was 1270 °C for 20 min. The composite materials were prepared by the combination of low carbon steel (LCS), high-density, large-sized WC particles and HCCI. Furthermore, traditional heat treatment process techniques were successfully applied to enhance the hardness and wear resistance of the matrix, and highly abrasion-resistant composites were prepared.

2. Materials and Methods

2.1 Materials

The chemical composition of the samples is listed in Table 1. WC particles and commercial LCS were used as parts to enhance wear resistance and toughness, respectively. The size of the LCS was 110 mm × 70 mm × 10 mm, and the surface was ground and cleaned with alcohol. Then, it was

Table 1 Chemical compositions of the composites (wt.%)

Material	C	Cr	Mn	Si	Ni	WC	Co	Fe
Matrix	2.50	16.08	0.80	0.60	0.90	Balance
WC	92	8	...
LCS	0.20	0.19	0.38	0.10	0.02	Balance

placed on the bottom of the corundum crucible (120 mm × 80 mm × 40 mm), as shown in Fig. 1. A three-dimensional blender was used to mix the matrix powder and WC particles evenly at a volume ratio of 60:40. The proportioned mix powders and the reinforced particles were preset on the surface of the LCS until they filled the entire corundum crucible and compacted it. Then, the samples were sintered in an atmosphere-protected resistance furnace (argon) at 1270 °C for 20 min.

All samples were heat-treated in a muffle furnace. The heat treatment process of the samples was as follows: all samples were held at 950 °C for 2 h, quenched in air (Q950), and then tempered at 220 °C (QT220), 350 °C (QT350), 400 °C (QT400) and 500 °C (QT500) for 120 min, respectively.

2.2 Microstructural Analysis

The microstructure of the samples was analyzed by field emission scanning electron microscopy (FE-SEM) with an Ultra Plus instrument (ZEISS). The element distribution of the diffusion layer region between the LCS and the WC/HCCI composite was studied by JXA-8530F EPMA. To determine the phase constitution of the samples, x-ray diffraction analysis was carried out on an X' Pert Pro PW3040/60 x-ray diffractometer (XRD). The samples were scanned in a 2θ range of 20°-90°, using Cu Kα radiation with a speed of 4.6°/min. Transmission electron microscopy (TEM) was implemented using a TENAI G20 transmission electron microscope at 200 kV.

2.3 Mechanical Property Testing

The microhardness distribution of the WC/HCCI composite region was acquired by a Vickers hardness tester using a 200 g load for 10 s. The impact toughness of the WC/HCCI samples and the LCS-toughened WC/HCCI samples were tested on a JBW-500 pendulum impact testing machine. With a size of 10 mm × 10 mm × 55 mm, the opening degree and opening depth of the sample were 45° and 2 mm, respectively. The shear tests were performed using a universal testing machine (IDW-200H) with a size of 10 mm × 10 mm × 55 mm.

The calculation formula of the shear strength was defined as $\sigma_K = \frac{F_x}{A_\mu}$, where σ_k is the shear strength (MPa), F_x is the ultimate load (N), and A_μ is the bonding area (mm²).

Using the ASTM-G65 standard, abrasive wear tests were performed on the MLG-130 dry sand/rubber wheel equipment. All samples were cut into a rectangular-shaped sample with a

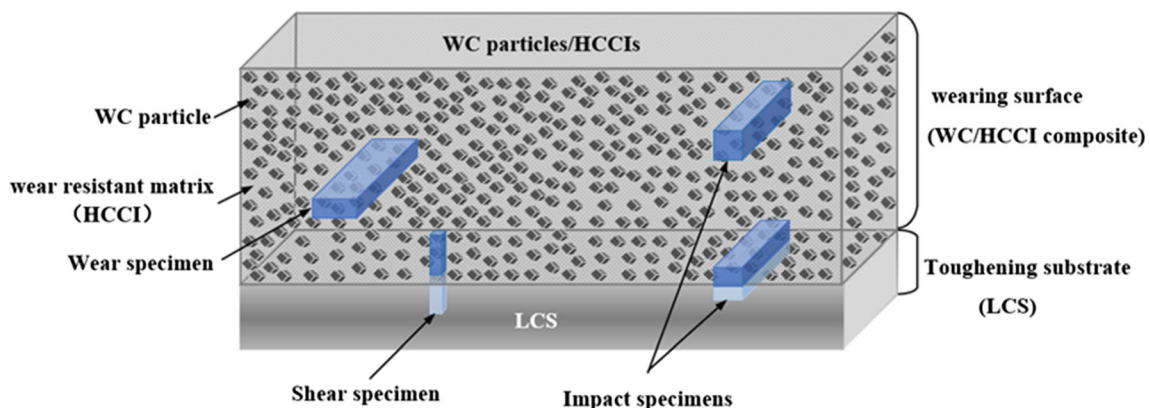


Fig. 1 The position of the test specimens for mechanical properties

size of 57 mm × 25.5 mm × 6 mm and loaded with 130 N. Silica sand of 50-70 mesh was used as wear medium at room temperature. The flow rate of the silica sand was kept constant at 300 g/min. The weightlessness of the samples was measured by an electronic balance at a sliding distance of 1400 m. The abrasive volume was defined as $\Delta V = \frac{\Delta M}{\rho}$, where ΔV is the abrasive volume (mm³), ΔM is the weight loss of the composites (g), and ρ is the density of the test material (g/cm³).

The sampling position of the mechanical properties of all samples is shown in Fig. 1.

3. Results and Discussion

3.1 Microstructure

The SEM micrographs of the WC/HCCI composites are shown in Fig. 2. There were no gaps or other defects between the WC particles (red circle symbols in Fig. 2a) and the HCCI matrix (blue triangle symbols in Fig. 2a), which indicated that the WC particle-reinforced HCCI composites were sintered well by LPS. In the as-cast composites, a small amount of WC particles was dissolved at the edge, which maintained the original WC particle size and maximized the wear resistance of the composites.

The visual size of the WC particles was 2.8 cm in length and 2.2 cm in width (Fig. 2a). To better observe the microstructures of WC particles and matrix, high-power SEM photographs were observed at the A and B frame areas in Fig. 2(a). As

shown in Fig. 2(b), the brighter part was tungsten carbides, and the dark part was the binder containing Co (Ref 19). Some of the WC particles were surrounded by a brighter phase, known to be W₂C. These M₂C-type carbides transformed from MC-type carbides during the LPS process. With the increase in local solubility of the WC particles, the C and W elements in the matrix had greatly increased, which promoted the formation of new high-W carbides in the matrix. The brighter phase of the SEM images was attributed to W carbides (Fig. 2c), which was verified by the chemical mapping of energy-dispersive spectroscopy (EDS). In addition, the W element can be converted not only into MC- and M₂C-type carbides (Fig. 2d) but also into eutectic carbides mainly formed by chromium (Ref 20).

The SEM microstructures of the composites are shown in Fig. 3. A great deal of MC-type and M₂C-type carbides with high-W proportions were retained in the as-cast composites (Fig. 3a). Due to the high content of alloy elements in the matrix of HCCI, part of the austenite was transformed into martensite during the cooling stage of the LPS process, but more residual austenite will be retained in the matrix of the room temperature structure (Fig. 3a1). Therefore, to convert the matrix into a highly alloyed martensite structure, the corresponding heat treatment of the material was required, including the WC/HCCI composites due to the existence of a large number of hard phases in these composites; when the carbide in the composite dissolved, it blocked the diffusion of iron and carbon atoms. These will hinder the formation or growth of austenite grains, thus increasing the formation temperature of austenite. Therefore, a quenching temperature of 950 °C was

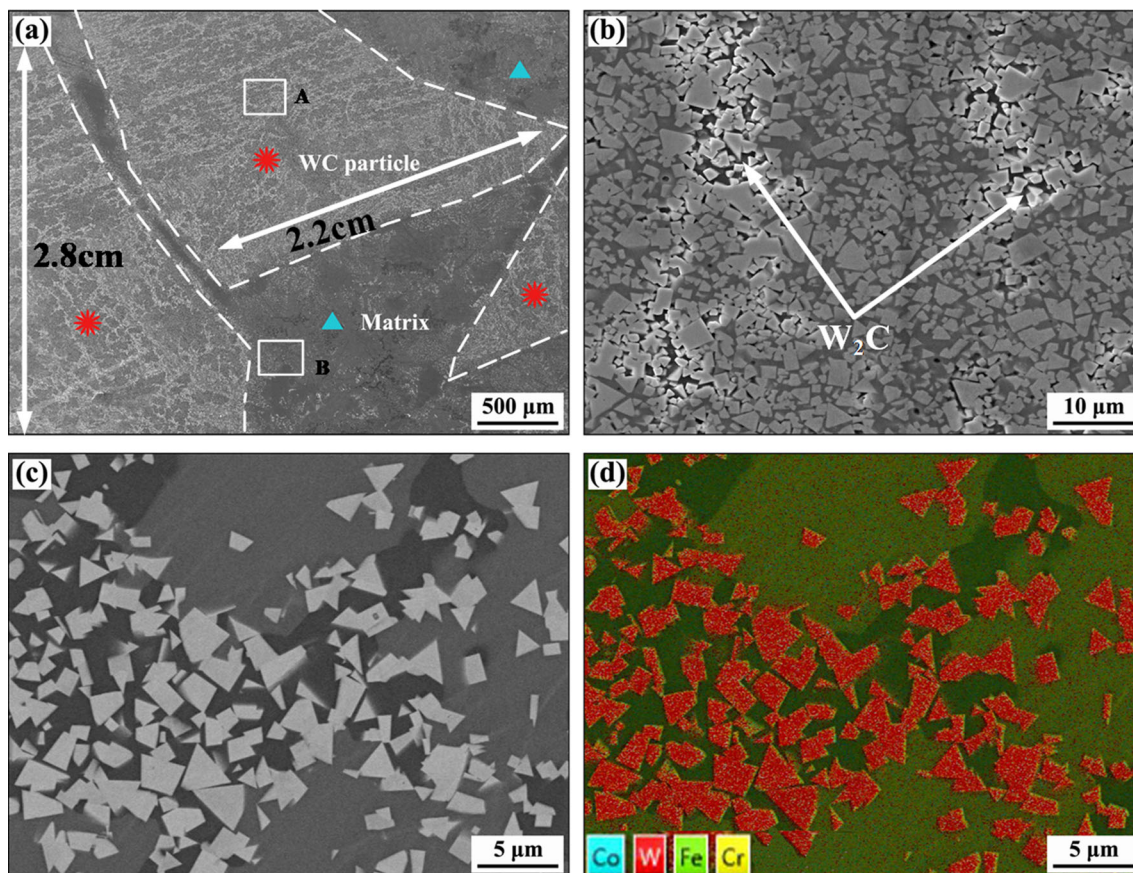


Fig. 2 (a) WC/HCCI composites; (b) WC particle; (c, d) Characterization of the HCCI matrix, as determined by EDS mapping under SEM

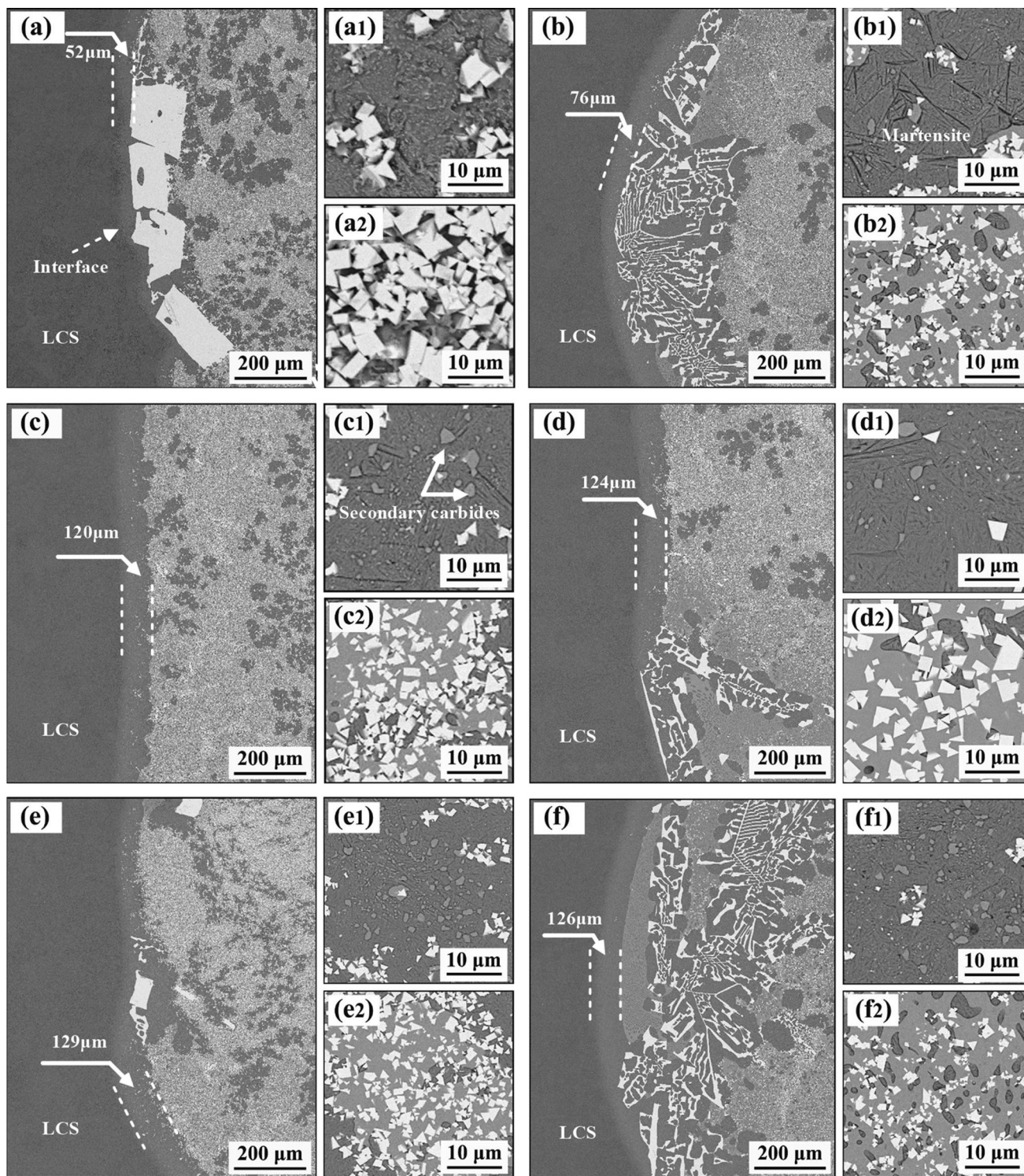


Fig. 3 SEM micrographs of LCS-toughened WC/HCCI composites in the as-cast and after different heat treatments conditions. (a, a1, a2) As-cast; (b, b1, b2) Q950; (c, c1, c2) QT220; (d, d1, d2) QT350; (e, e1, e2) QT400; (f, f1, f2) QT500

used in this study, as shown in Fig. 3(b), and the matrix of the composite material was significantly martensified (Fig. 3b1). After quenching, the MC-type and M_2C -type carbides were still distributed in the interior or grain boundary of the original grain after tempering the experimental samples at four different temperatures of 220 °C, 350 °C, 400 °C and 500 °C. With the increase in tempering temperature, the WC particles and the

HCCI matrix dissolved and precipitated with each other through diffusion, but the WC particles only slightly dissolved. On the one hand, this dissolution weakened the sharp angle of the WC particles and improved the interface bonding strength between the WC particles and the HCCI matrix; on the other hand, the diffusion of elements promoted the formation of secondary carbides, which further improved the wear resistance

of the composites. It can be seen from Fig. 3(a2), (b2), (c2), (d2), (e2), (f2) that heat treatment has little effect on the morphology of WC particles, and they have always existed in the composite materials as triangles or quadrilaterals (Ref 21). The microstructure changes after heat treatment were mainly reflected in the HCCI matrix, which showed the decomposition of martensite, the segregation and uniform distribution of secondary carbides and the dissolution and precipitation of carbides.

Under the condition of QT220 (Fig. 3c), there were strip structures, gray block structures and white triangles or multi-lateral structures in the matrix of the composites, and its matrix was cryptocrystalline tempered martensite, secondary carbides and W-rich carbides. According to the XRD analysis (Fig. 4), the secondary carbides were mainly $M_{23}C_6$ types, and the W-rich carbides were Fe_3W_3C compound carbides. At the lower tempering temperatures, the structure of cryptocrystalline martensite was obvious, the secondary carbides started to precipitate out, and the particle size showed the combination of large particles and small particles (Fig. 3c1).

Figure 3(d) highlights that under QT350 heat treatment conditions, the martensite structure in the composite matrix was partly ambiguous and disordered. The size of particles of secondary carbides in the matrix was still different, and there was a certain degree of segregation (Fig. 3d1).

After QT400 heat treatment (Fig. 3e), the martensitic structure began to become ambiguous (Fig. 3e1). When tempering at high temperature of 400 °C, the edge solubility of the WC particles increased, and the alloy elements thus precipitated in the form of secondary carbides in the matrix due to supersaturation, such as that of a white granular structure (Fe_3W_3C compound carbides) and of $M_{23}C_6$ -type carbides. In addition, the size of secondary carbide particles in the matrix tended to be the same, their roundness was enhanced, and they were distributed uniformly in the matrix (Fig. 3e1).

When the tempering temperature reached 500 °C (QT500), the martensite structure appeared ambiguous or even disappeared, while the secondary carbide content in the matrix of the composites increased (Fig. 3f). The reason for this phenomenon was that the carbon and chromium elements in the matrix and the dissolved W element from the WC particles

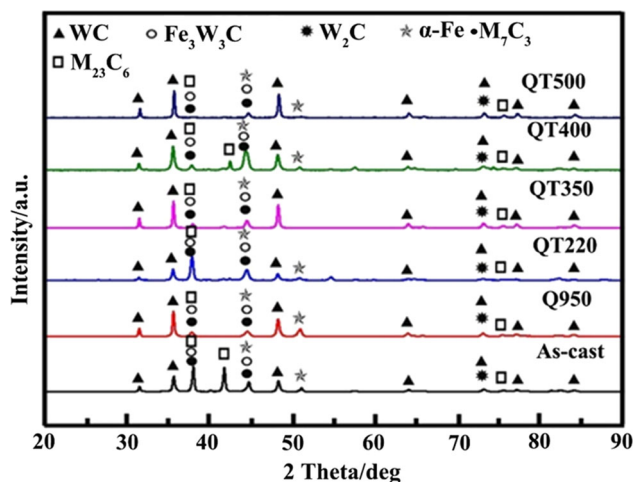


Fig. 4 X-ray diffraction of the composites before and after heat treatment

contributed to the formation of secondary carbides at higher tempering temperatures. In the subsequent cooling process, with the increase in secondary carbides, the supersaturation and excessive precipitation of carbon atoms in the martensite matrix reduced the lattice distortion of martensite, resulting in weakening of the matrix strength (Fig. 3f1).

To maximize the size of the original WC particles and ensure effective metallurgical interface bonding, a sintering process with a sintering temperature of 1270 °C for 20 min was adopted in this experiment. The LCS and WC/HCCI are the two sides of the interface in the composites (Fig. 5a). Figure 5(b), (c), (d), and (e) shows the corresponding surface scan distributions of the C, Cr, W, and Fe elements, respectively. According to the Fe-C phase diagram, when the low-carbon steel is in the austenite region, the Cr and W atoms with a larger atomic radius did not diffuse into the austenite through the tetrahedral gap or the octahedral gap, but they appeared in the diffusion layer. In terms of crystallography, the interface between the reinforcing particles and the matrix in the composites is often an incoherent high-energy interface, so they serve as very effective vacancy sources that provide a fast diffusion channel of those atoms in the layer (Ref 22). As shown in Fig. 3, the W element in the reinforced particles appeared in the diffusion layer, and the original concentration of the W element in the original LCS was 0, and the concentration of the tungsten carbide remained unchanged throughout the process on the LCS surface. The LCS can be regarded as a semi-infinite object, and the diffusion coefficient was independent of the concentration (Ref 23), according to Fick's second law:

$$c = c_0 \left(1 - \operatorname{erf} \frac{x}{2\sqrt{D\tau}} \right) \quad (\text{Eq 1})$$

where c is the concentration (wt.%) of the diffusion enhancer at the contact surface χ between the LCS and the reinforcing region after τ time (%), c_0 is the ultimate concentration (wt.%) of the diffuser in the LCS, and D is the diffusion coefficient. Since the size of the LCS is much larger than $2\sqrt{D\tau}$, it can be regarded as an infinite one-dimensional diffusion, as shown in Fig. 5(f). When $c_x = 0$, c_0 is the limiting concentration of the enhancer in the LCS. The semidiffusion activation energy of the W element in austenite is $E_a = 261.5$ kJ/mol, and the self-diffusion constant of the W element is $A_0 = 42.80$ cm²/s, which can be used to determine the rate constant according to the Arrhenius equation (Ref 24):

$$D_T = A_0 e^{-E_a/RT} \quad (\text{Eq 2})$$

where D is the rate constant, R is the molar gas constant, T is the thermodynamic temperature, and E_a is the semidiffusion activation energy of the elements in austenite. When the sintering temperature was 1270 °C and the gas constant $R = 8.31$ J/K, the diffusion coefficient of the WC particles was calculated as $D_T = 7.42 \times 10^{-10}$ cm²/s.

At a distance from the WC particles, the WC particle concentration in the LCS can be considered to be zero; therefore,

$$\operatorname{erf} \frac{x}{2\sqrt{D\tau}} = 1, \quad (\text{Eq 3})$$

$$\text{then } x = 5.6\sqrt{D\tau}. \quad (\text{Eq 4})$$

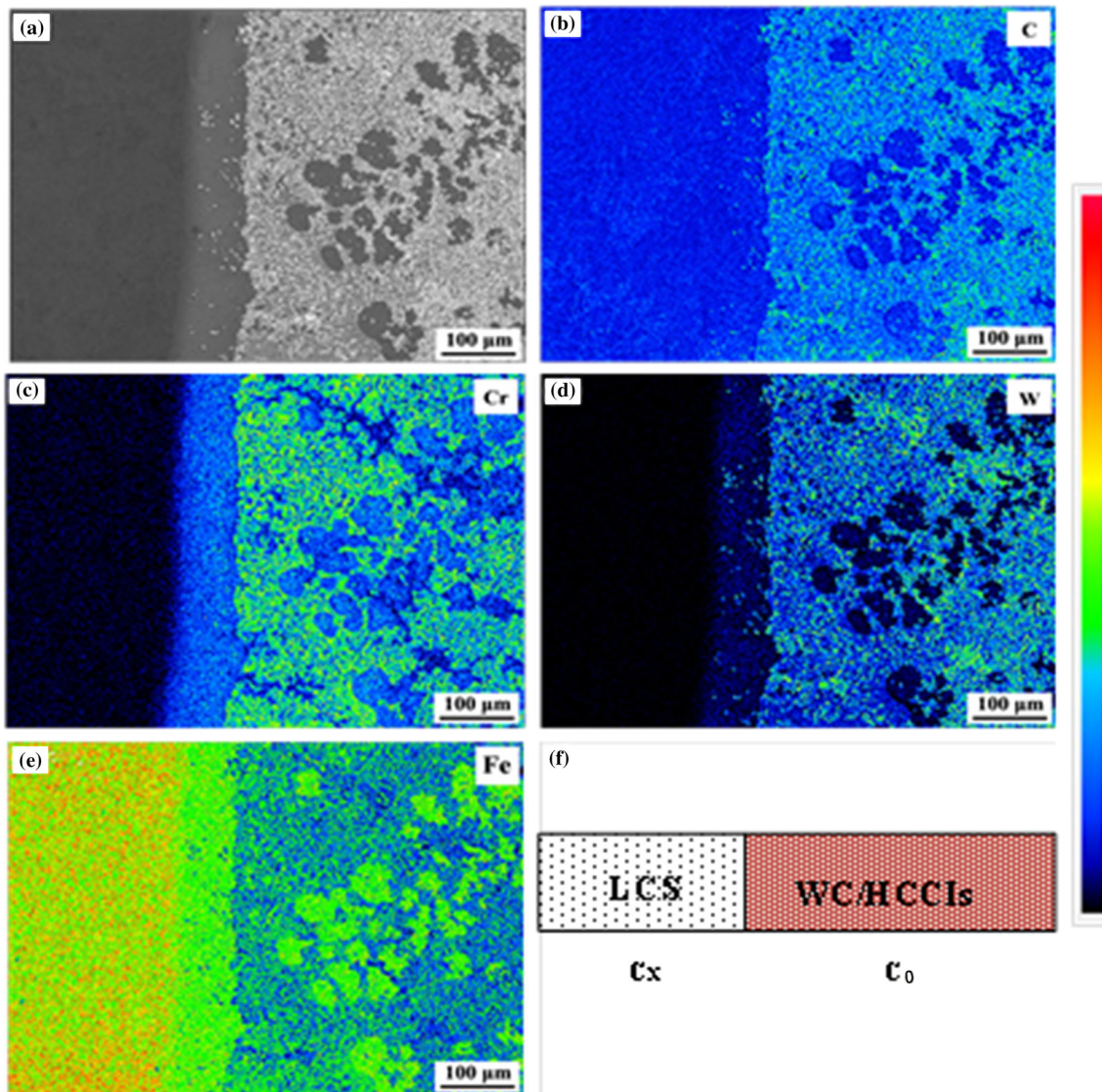


Fig. 5 Surface scanning analysis of composites by EPMA: (a) microscopy of back-scattered electrons; (b) C; (c) Cr; (d) W; (e) Fe; (f) one-dimensional diffusion diagram

During the heat preservation phase and cooling process of vacuum LPS, the temperature changes with time and affects the diffusion coefficient. Assuming that the temperature is linear with time, the diffusion coefficient is also linear with temperature. The average temperature at which the sample is cooled from 1543 to 1000 K is the average temperature for elemental diffusion, because the diffusion coefficient of the W element is very small at less than 1000 K ($1 \times 10^{-12} \text{ cm}^2/\text{s}$). Therefore, in this study the average cooling time was 40 min, and the holding time was 20 min, which was approximately 60 min in total.

In the as-cast structure, the diffusion thickness of the W element is:

$$\tau = 60 \text{ min}, x = 52.8 \mu\text{m}.$$

After the composite material was heat-treated, the holding time was 120 min. The theoretical diffusion temperature of the W element is:

$$\tau = 120 \text{ min}, x = 129 \mu\text{m}.$$

The thickness of the diffusion layer of the as-cast and heat-treated composites was 50 and 120 ~ 129 μm , respectively. The calculated data were basically consistent with the theoretical data.

The final structure mainly consisted of a martensite matrix, which was reinforced by secondary carbides and unchanged carbides, such as M_7C_3 -type, M_6C -type and MC-type carbides. Combined with XRD (Fig. 4) and TEM-EDS analysis (Fig. 6a and b), it can be confirmed that the black area of the quadrilateral or triangle was tungsten carbide (Fig. 6a, area A), and the white-gray region was α -Fe, with a small amount of W and Cr. In the Fe-W-C phase diagram, the C, W and Cr elements were supersaturated in the α -Fe region (Area C in Fig. 6a) (Ref 20). This suggests that the element distribution of Fe, Cr, and W in the matrix could form both the low-W-(Cr, Fe) xC_y phase (Area B in Fig. 6a) and the chromium carbide-based

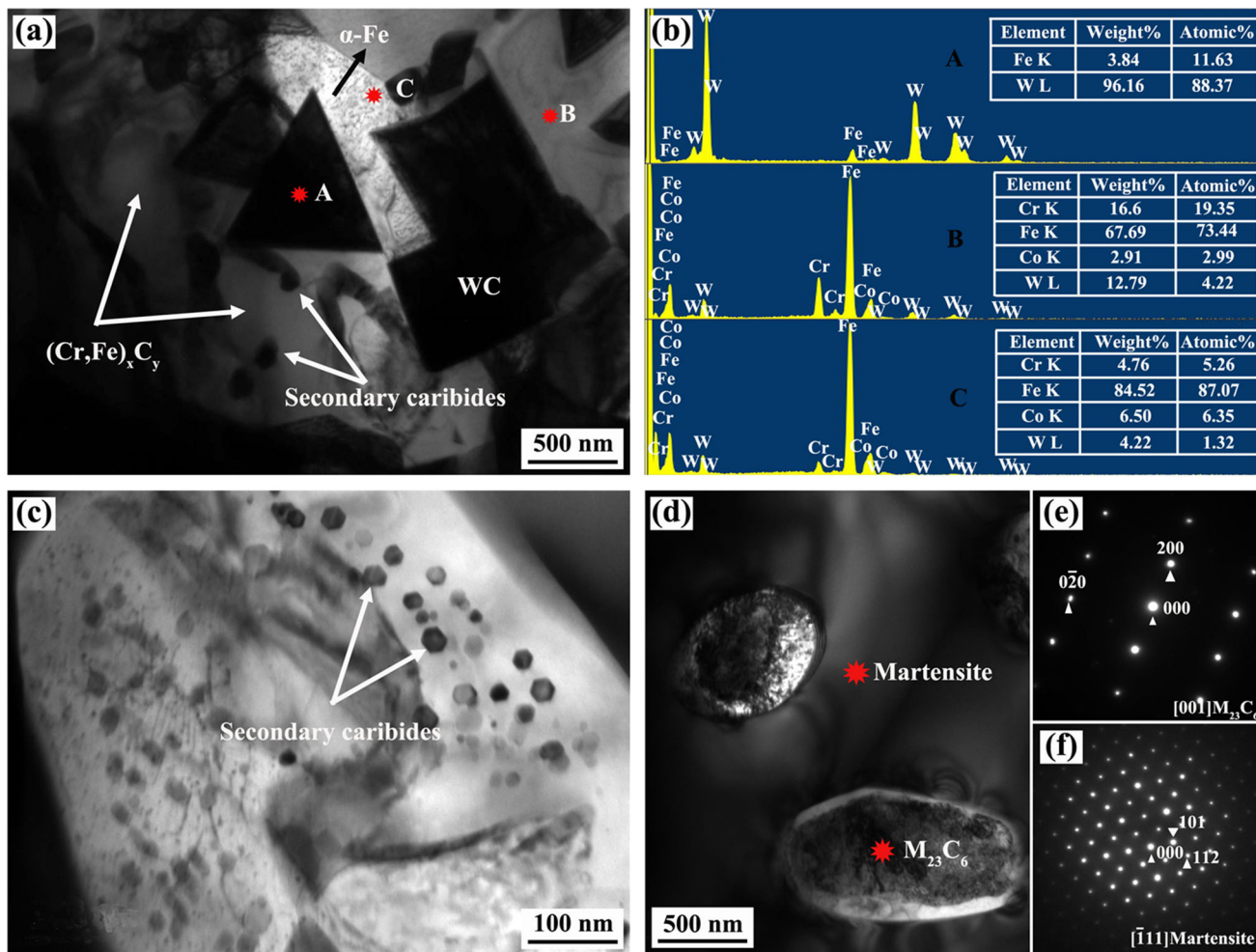


Fig. 6 TEM analysis of the WC/HCCI composite. (a) TEM image of the WC/HCCI composite, (b) TEM-EDS results, (c, d) BF-TEM micrograph show the microstructure of the WC/HCCI composite, (e, f) corresponding SADPs from the $[001]$ $M_{23}C_6$ zone axis and $[\bar{1}11]$ Martensite zone axis

phase ($M_{23}C_6$ carbides). These secondary carbides have a relatively regular spherical shape, which mitigates stress concentration due to the sharp corners of the polygonal carbide, reducing the tendency of crack initiation, and acting as a second phase-strengthening effect in the matrix (Fig. 6c and d). In this paper, the secondary carbide and the matrix electron diffraction spots were calibrated to determine the $M_{23}C_6$ -type carbides and the martensite matrix (Fig. 6e and f).

3.2 Hardness

The microhardness of the as-cast and different heat-treated samples in different regions is shown in Fig. 7. By comparing the microhardness of the WC particles in the as-cast and heat-treated composites, it was found that the microhardness of the WC particles changed only slightly. Combined with SEM micrograph analysis, the surface solubility of the WC particles was observed to increase under different heat treatment conditions. However, as a result of the large particle size of reinforced particles, they could not completely diffuse and dissolve, and the internal hardness loss was small. Similarly, we also know that the M_7C_3 -type and $M_{23}C_6$ -type carbides were also relatively stable and difficult to change under heat treatment conditions.

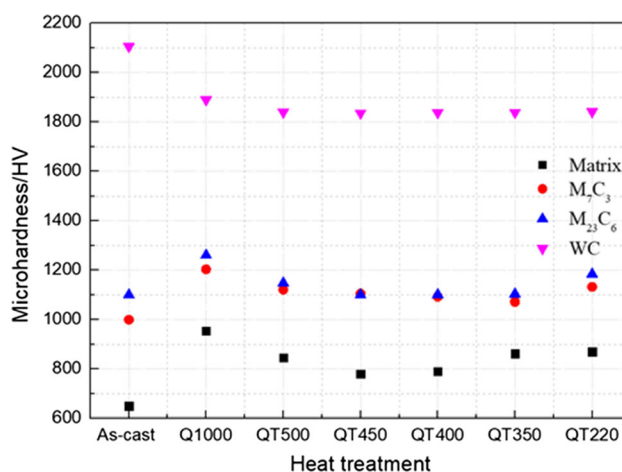


Fig. 7 Microhardness of composite materials in different regions before and after heat treatments

To analyze the influence of heat treatment on the microhardness of the composites, the microhardness of the matrix was measured. The results show that the hardness of the matrix was greatly improved under different tempering conditions

after quenching at 950 °C. At different tempering temperatures, the microhardness of the matrix first increased and then decreased. The main reason was that the matrix mainly existed in the form of martensite, and few secondary carbides were precipitated when tempered at 220 °C. However, when the tempering temperature was high, secondary carbide precipitation increased, resulting in an abundance of supersaturated C atom precipitation in the martensite, resulting in a decrease in the microhardness of the matrix.

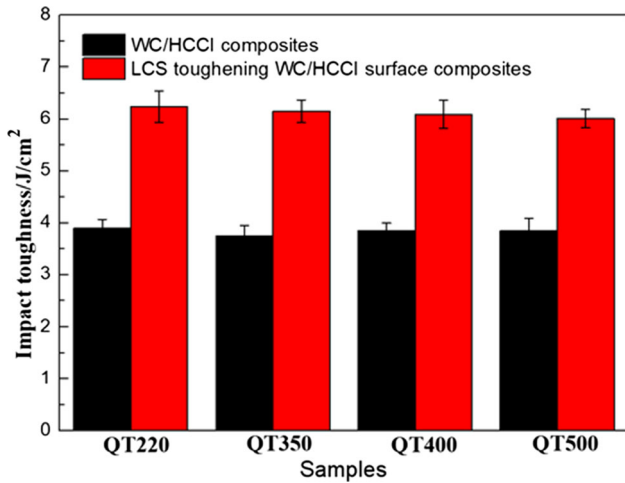


Fig. 8 Impact toughness values of WC/HCCIs composites and LCS-toughened WC/HCCI composites after different heat treatments

3.3 Impact Toughness

The impact toughness values of the composites are shown in Fig. 8. The impact toughness value of the WC/HCCI composites was low, ranging from 3.8 to 3.9 J/cm². The impact toughness value of the composites did not change after different heat treatment processes. However, the LCS-toughened WC/HCCI composites greatly improved (as shown in the red histogram in Fig. 8).

The fracture morphologies of those samples were typical cleavage fractures and partial dimple fractures (Fig. 9a, b and c). The size of the WC particles has an important influence on the plastic deformation and hardening behavior of the material. Because the WC particle size was 2 to 3 mm and the volume fraction was 40%, the materials were brittle. Under the action of external force, the matrix underwent plastic deformation, and the stress concentrated at the particles. The larger the particle size, the more dislocations and the greater the stress concentration (Ref 25). Under the action of a small impact stress, the cleavage fracture of particles can occur as shown in Fig. 9(c). River patterns have obvious cleavage fracture characteristics (Fig. 9b), and there were obvious dimples in the matrix, which indicated the toughness characteristics present in the composites.

3.4 Shear Test

Shear strength tests are often used to evaluate the interfacial bond strength of two materials. Bowen Xiong et al. (Ref 26) fabricated high-chromium cast iron and medium-carbon steel bimetal by liquid–solid casting in an electromagnetic induction

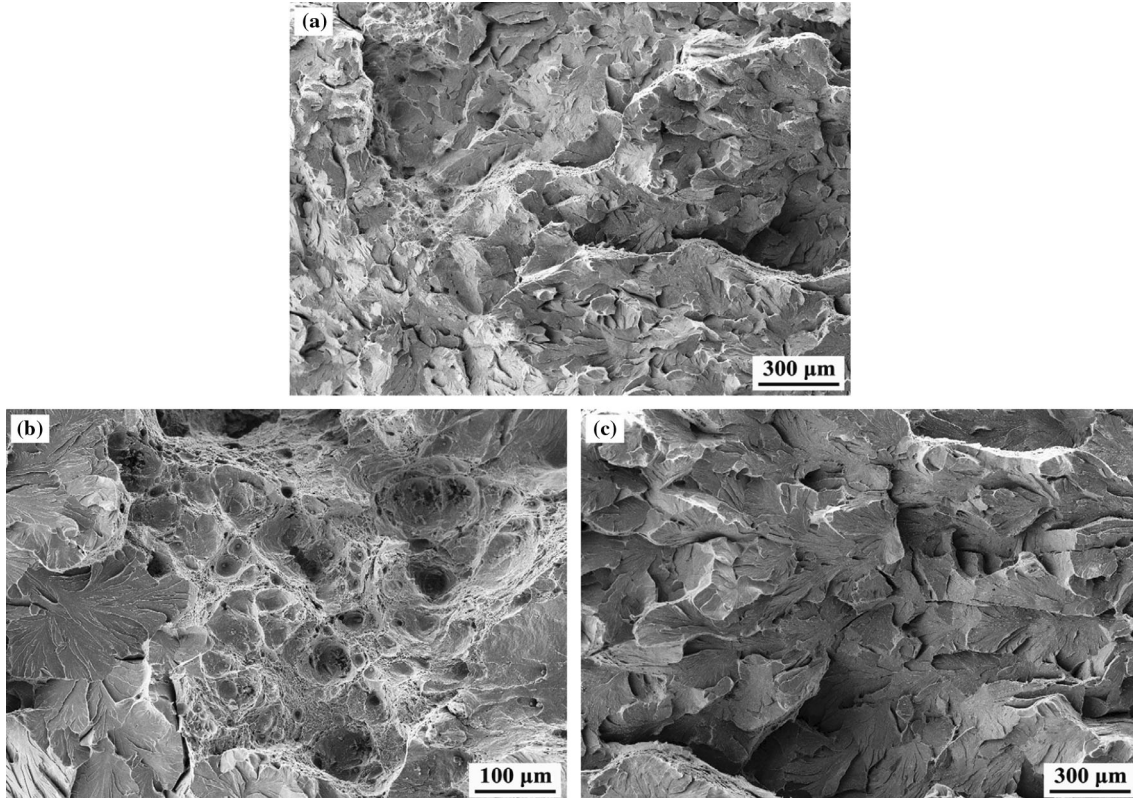


Fig. 9 SEM fractography of impact test specimen. (a) As-cast WC/HCCI composites; (b) the area of HCCI; (c) the area of WC particles

field, which gave an interface shear strength of 281.2 MPa, and that fabricated by conventional processes was only 236.2 MPa. The shear strength of the as-cast composites in this experiment was 100.9 MPa, and the shear strength value at the interface joint after heat treatment significantly increased, reaching a maximum value of 202.36 MPa (Fig. 10). Compared with the research results of other scholars, the shear strength value of this paper was relatively low, mainly because there were a large

number of brittle materials in the composite materials. Although there was no obvious dominant value, the shear strength still proved that there was a certain bonding strength between the two materials. In this paper, reducing the quenching temperature and tempering temperature eliminated the internal stress of the material but did not promote the fracture of the material. In addition, under the condition of a low tempering temperature, the secondary carbides in the

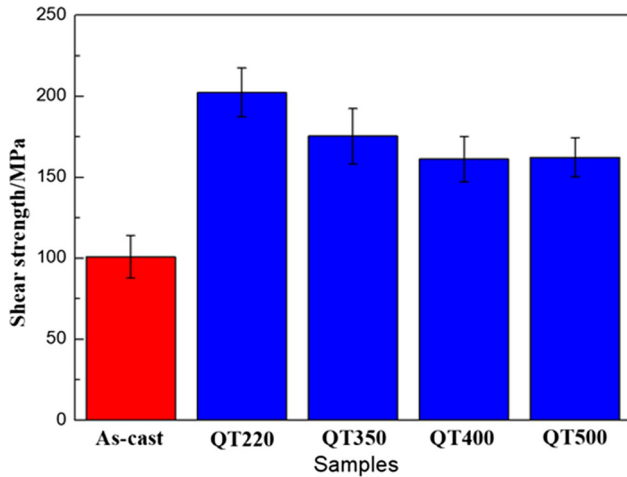


Fig. 10 Shear strength values of LCS-toughened WC/HCCI composites before and after different heat treatments

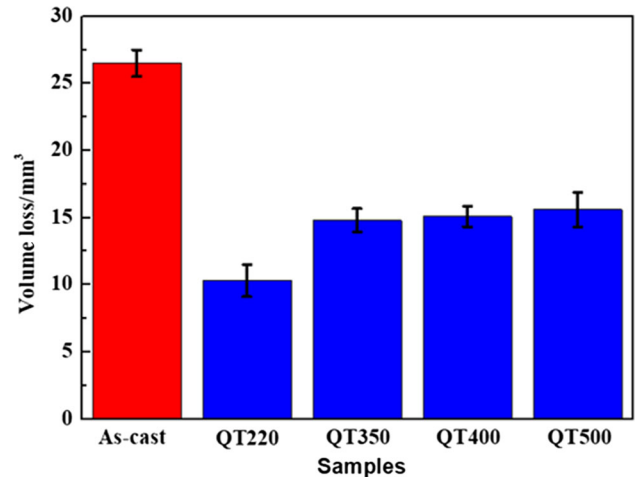


Fig. 12 Volume-loss values of WC/HCCI composites before and after different heat treatments

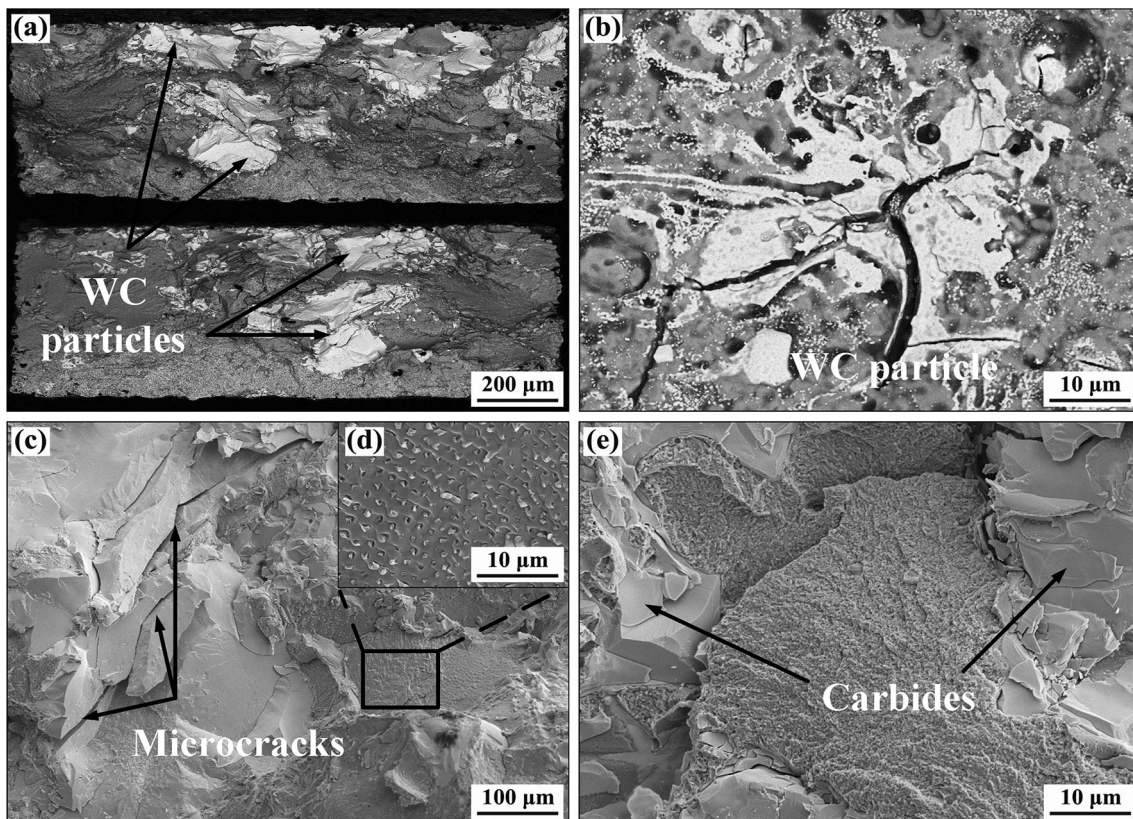


Fig. 11 SEM fractography of shear strength test specimen. (a) Macroscopic fracture morphology of shear strength test specimen; (b) detail of the WC particle at the fracture; (c-e) Fracture morphology of WC/HCCI composite

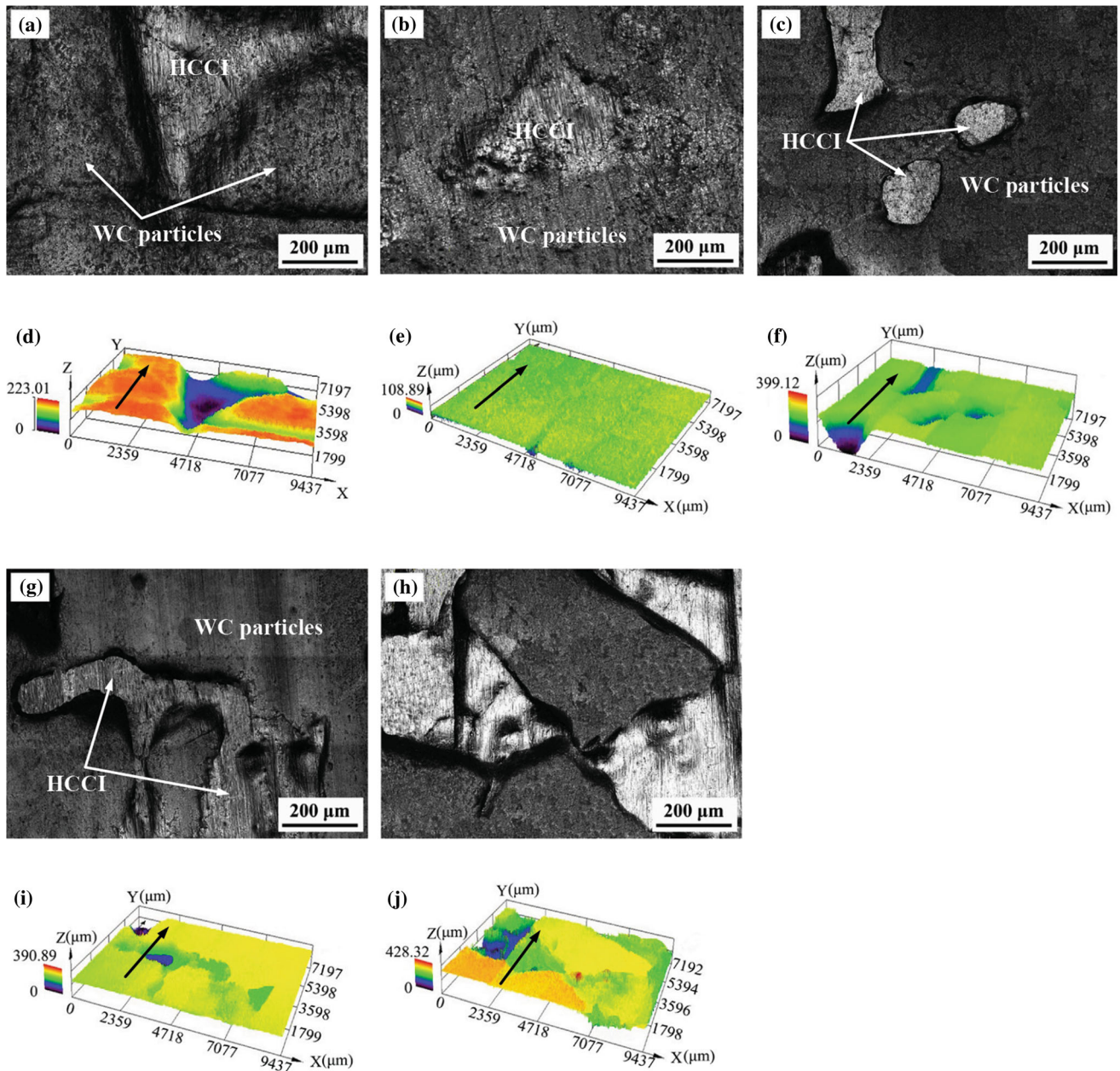


Fig. 13 Wear surface analysis of WC/HCCI composites after different heat treatments by Laser Scanning Confocal Microscopy micrographs. (a) As-cast and (d) is the corresponding 3D digital image, (b) QT220 and (e) is the corresponding 3D digital image, (c) QT350 and (f) is the corresponding 3D digital image, (g) QT450 and (i) is the corresponding 3D digital image, (h) QT500 and (j) is the corresponding 3D digital image

matrix were less precipitated, and the matrix structure was a large number of tempered martensite, which plays a protective role against the carbides.

The macroscopic topography of the interface shear fracture of LCS-toughened WC/HCCI composites is shown in Fig. 11. The large-scale transgranular fracture of WC particles showed that the fracture region was on the side of WC/HCCI composites and did not occur at the interface between the LCS and the WC/HCCI composites or on the LCS side (Fig. 11a and b). The results showed that the LCS and the WC/HCCI interface composite effect was better. Figure 11(c) shows

the obvious cleavage steps and river patterns, and multiple secondary cracks are distributed on the fracture, showing transgranular fractures and intergranular fractures. Figure 11(d) shows that a large number of carbides rich in W and Cr were formed in the matrix, which had a greater effect on the interfacial shear strength of those composites. The WC particles showed obvious large cracks and a large number of broken pieces of rock sugar, showing the characteristics of intergranular fracture. The matrix for joining the WC particles is shown in Fig. 11(e). The interfacial shear strength of the composites was greatly affected by the microstructure of the matrix and the

number and size of the newly formed secondary carbides in the matrix.

3.5 Abrasive Wear Resistance

For wear-resistant materials, the wear rate is an important criterion for measuring the performance of materials. In this paper, abrasive wear tests of the WC/HCCI composites with different heat treatments were carried out. Figure 12 shows the volume loss of the composites. The volume loss of the as-cast composites after the abrasive wear test was 26.5 mm³. After quenching at 950 °C and tempering at 220 °C, the volume loss decreased to 10.3 mm³. It is worth noting that the wear resistance of the WC/HCCI composites formed under heat treatment conditions was 5 times that of the as-cast composites. This indicates that although the WC particles can exhibit excellent wear resistance in the composites, the whole material cannot achieve this, as the wear resistance of the matrix is far from that of the WC particles. In long-term harsh environments, the matrix material cannot be coated with WC particles because of its insufficient wear resistance. Some authors (Ref 27, 28) have reported that when the friction forces are high enough for the matrix to move, most carbides are easily cracked or fall off with the softer matrix.

The surface analysis of the as-cast WC/HCCI composites and the WC/HCCI composites produced under different heat treatment processes was carried out by laser confocal microscopy, as shown in Fig. 13(a), (b), (c), (g), and (h). By comparing the worn surface topography, the volume loss of the HCCI matrix without heat treatment was larger, and the color ratio shown below the three-dimensional digital images can be seen, and the black arrow direction was the sliding direction of the wear (Fig. 13d, e, f, i, and j). The WC particles protruded completely from the worn material surface, and the particles did not appear to fall off and break. The grooves on the WC particles were very shallow, indicating that the abrasive particles were sliding on the WC particles, but varying degrees of scratches on the surface of the matrix material were exhibited. Therefore, the smaller the wear difference between the matrix material and the WC particles, the more effective the cutting resistance of WC particles to quartz particles, thus effectively protecting the matrix material.

4. Conclusions

In this paper, millimeter WC particles were used as reinforcing phases to prepare composite materials. Their microstructures and excellent properties were studied. Thus, we can draw the following conclusions.

- (1) The millimeter WC particle/HCCI and LCS composites were successfully prepared by liquid-phase sintering. The initial mechanical properties of the WC particles were retained by a small amount of dissolution at the edge of the original WC particles.
- (2) The main phases in the composites were ferrite, MC, M₂C, M₆C, M₇C and M₂₃C₆. The WC/HCCI composite had a strong interface with the LCS. After heat treatment, the interface width of the two components ranged from 120 to 129 μm, and the shear strength of the interface reached 202.36 MPa.

- (3) The wear properties of WC/HCCI composites after heat treatment of QT220 exhibited excellent wear resistance (10.3 mm³).

Acknowledgments

This research was supported by the National Natural Science Foundation of China (U1810109).

References

1. R. Khoshhal, M. Soltanieh, and M.A. Boutorabi, Formation Mechanism and Synthesis of Fe-TiC/Al₂O₃ Composite by Ilmenite, Aluminum and Graphite, *Int. J. Refract. Met. Hard Mater.*, 2014, **45**, p 53–57
2. J. Ru, H. He, Y. Jiang, R. Zhou, and Y. Hua, Wettability and Interaction Mechanism for Ni-Modified ZTA Particles Reinforced Iron Matrix Composites, *J. Alloys Compd.*, 2019, **786**, p 321–329
3. J. Nurminen, J. Näkki, and P. Vuoristo, Microstructure and Properties of Hard and Wear Resistant MMC Coatings Deposited by Laser Cladding, *Int. J. Refract. Met. Hard Mater.*, 2009, **27**, p 472–478
4. R. Zhou, Y. Jiang, and D. Lu, The Effect of Volume Fraction of WC Particles on Erosion Resistance of WC Reinforced Iron Matrix Surface Composites, *Wear*, 2003, **255**, p 134–138
5. J. Ru, Y. Jiang, R. Zhou, J. Feng, Y. Hua, and Q. Yang, Preparation of Ni-Encapsulated ZTA Particles as Precursors to Reinforce Iron-Based Composites, *Adv. Eng. Mater.*, 2017, **19**, p 1–11
6. C.M. Fernandes, L.M. Vilhena, C.M.S. Pinho, F.J. Oliveira, E. Soares, J. Sacramento, and A.M.R. Senos, Mechanical Characterization of WC-10 wt% AISI, 304 Cemented Carbides, *Mater. Sci. Eng. A*, 2014, **618**, p 629–636
7. J.I. Verdeja, J. Asensio, and J.A. Pero-Sanz, Texture, Formability, Lamellar Tearing and HIC Susceptibility of Ferritic and Low-Carbon HSLA Steels, *Mater. Charact.*, 2003, **50**, p 81–86
8. S.H.M. Anijdan, A. Bahrami, N. Varahram, and P. Davami, Effects of Tungsten on Erosion-Corrosion Behavior of High Chromium White Cast Iron, *Mater. Sci. Eng. A*, 2007, **454–455**, p 623–628
9. E. Ghasali, T. Ebadzadeh, M. Alizadeh, and M. Razavi, Spark Plasma Sintering of WC-Based Cermets/Titanium and Vanadium Added Composites: A Comparative Study on the Microstructure and Mechanical Properties, *Ceram. Int.*, 2018, **44**, p 10646–10656
10. A.J. Cavaleiro, C.M. Fernandes, A.R. Farinha, C.V. Gestel, J. Jhabvala, E. Boillat, A.M.R. Senos, and M.T. Vieira, The Role of Nanocrystalline Binder Metallic Coating into WC After Additive Manufacturing, *Appl. Surf. Sci.*, 2017, **427**, p 131–138
11. Z. Li, Y. Jiang, R. Zhou, F. Gao, Q. Shan, and J. Tan, Thermal Fatigue Mechanism of WC Particles Reinforced Steel Substrate Surface Composite at Different Thermal Shock Temperatures, *J. Alloys Compd.*, 2014, **596**, p 48–54
12. N. Espallargas, J. Berget, J.M. Guilemany, A.V. Benedetti, and P.H. Suegama, Cr₃C₂-NiCr and WC-Ni Thermal Spray Coatings as Alternatives to Hard Chromium for Erosion-Corrosion Resistance, *Surf. Coat. Technol.*, 2008, **202**, p 1405–1417
13. H. Peng, H. Guo, J. He, and S. Gong, Oxidation and Diffusion Barrier Behaviors of Double-Layer NiCoCrAlY Coatings Produced by Plasma Activated EB-PVD, *Surf. Coat. Technol.*, 2011, **205**, p 4658–4664
14. A. Genç, E. Ayas, M.L. Öveçoğlu, and S. Turan, Fabrication of In Situ Ni(W)-WC Nano Composites via Mechanical Alloying and Spark Plasma Sintering, *J. Alloys Compd.*, 2012, **542**, p 97–104
15. C.M. Fernandes, A.M.R. Senos, and M.T. Vieira, Sintering of Tungsten Carbide Particles Sputter-Deposited with Stainless Steel, *Int. J. Refract. Met. Hard Mater.*, 2003, **21**, p 147–154
16. C.M. Fernandes, A.M.R. Senos, and M.T. Vieira, Control of Eta Carbide Formation in Tungsten Carbide Powders Sputter-Coated with (Fe/Ni/Cr), *Int. J. Refract. Met. Hard Mater.*, 2007, **25**, p 310–317
17. S.H. Chang, M.H. Chang, and K.T. Huang, Study on the Sintered Characteristics and Properties of Nanostructured WC-15 wt%(Fe-Ni-Co) and WC-15 wt% Co Hard Metal Alloys, *J. Alloys Compd.*, 2015, **649**, p 89–95

18. S.H. Chang and P.Y. Chang, Study on the Mechanical Properties, Microstructure and Corrosion Behaviors of Nano-WC-Co-Ni-Fe Hard Materials Through HIP and Hot-Press Sintering Processes, *Mater. Sci. Eng. A*, 2014, **618**, p 56–62
19. T. Yang, Q. Wei, Q. Yao, Y. Wang, Y. Xie, J. Luo, and Z. Yu, Microstructure Evolution of Thermal Spray WC-Co Interlayer During Hot Filament Chemical Vapor Deposition of Diamond Thin Films, *J. Alloys Compd.*, 2015, **639**, p 659–668
20. M. Tarraste, J. Kübarsepp, K. Juhani, A. Mere, M. Koinen, M. Viljus, and B. Maaten, Ferritic Chromium Steel as Binder Metal for WC Cemented Carbides, *Int. J. Refract. Met. Hard Mater.*, 2018, **73**, p 183–191
21. D. Gu and W. Meiners, Microstructure Characteristics and Formation Mechanisms of In Situ WC Cemented Carbide Based Hardmetals Prepared by Selective Laser Melting, *Mater. Sci. Eng. A*, 2010, **527**, p 7585–7592
22. Y. Li, M. Gong, K. Wang, P. Li, Y. Xu, and W. Tong, Diffusion Behavior and Mechanical Properties of High Chromium Cast Iron/Low Carbon Steel Bimetal, *Mater. Sci. Eng. A*, 2018, **718**, p 260–266
23. L. Zhang and N.P. Padture, Inhomogeneous Oxidation of ZrB₂-SiC Ultra-high-temperature Ceramic Particulate Composites and Its Mitigation, *Acta Mater.*, 2017, **129**, p 138–148
24. M. Zhou, Y. Jiang, and Y. Sui, Microstructure and Properties of Interfacial Transition Zone in ZTA Particle-Reinforced Iron Composites, *Appl. Phys.*, 2019, **125**, p 110–120
25. J. Wang, L. Li, and W. Tao, Crack Initiation and Propagation Behavior of WC Particles Reinforced Fe-Based Metal Matrix Composite Produced by Laser Melting Deposition, *Opt. Laser Technol.*, 2016, **82**, p 170–182
26. B. Xiong, C. Cai, H. Wan, and B. Lu, Fabrication of High Chromium Cast Iron and Medium Carbon Steel Bimetal by Liquid-Solid Casting in Electromagnetic Induction Field, *Mater. Des.*, 2011, **32**, p 2978–2982
27. A. Bedolla-Jacuinde, F.V. Guerra, I. Mejía, and J. Zuno-Silva, Abrasive Wear of V-Nb-Ti Alloyed High-Chromium White Irons, *Wear*, 2015, **332–333**, p 1006–1011
28. E. Cortés-Carrillo, A. Bedolla-Jacuinde, I. Mejía, C.M. Zepeda, J. Zuno-Silva, and F.V. Guerra-Lopez, Effects of Tungsten on the Microstructure and on the Abrasive Wear Behavior of a High-Chromium White Iron, *Wear*, 2017, **376–377**, p 77–85

Publisher's Note Springer Nature remains neutral with regard to jurisdictional claims in published maps and institutional affiliations.